Supporting Information

Stabilizing Layered Sr-Intercalated CoO_2 Nanotubes for Bifunctional Energy Applications: Enhanced OER Catalysis and Energy Storage

Rajat Kumar Mohanta[a] *, Radha Somaiya[b,c], Sanika S. Padelkar[d,e,f,g], Aftab Alam[d,e], Aswani Yella[h] * and Leela S. Panchakarla[a †]

a. Department of Chemistry, Indian Institute of Technology Bombay, Powai, Mumbai-400076
b. School of Physics and Electronics, Hunan University, Changsha, 410082, China
c. Department of Chemistry, Davidson School of Chemical Engineering, Purdue University, West Lafayette, IN 47907, USA
d. Department of Physics, Indian Institute of Technology Bombay, Powai, Mumbai-400076
e. IITB-Monash Research Academy, Indian Institute of Technology Bombay, Powai, Mumbai-400076
f. School of Chemistry, Monash University, Melbourne, Victoria, 3800, Australia
g. Department of Materials Science and Engineering, Monash University, Melbourne, Victoria, 3800, Australia
h. Department of Metallurgical Engineering & Materials Science, Indian Institute of Technology Bombay, Powai, Mumbai-400076

e-mail: mohantarajat436@gmail.com, aswani.yella@iitb.ac.in

† Prof. Leela S Panchakarla sadly passed away

METHODS SECTION

4.1 Synthesis of bulk $Sr_6Co_5O_{15}$ (SCO bulk)

Bulk $Sr_6Co_5O_{15}$ was synthesized by sol-gel method, strontium nitrate tetrahydrate and cobalt nitrate hexahydrate were mixed in a 6:5 ratio with MilliQ water. The resulting solution was heated to 90 °C for one hour to make it concentrated gel, then poured into an alumina boat. This container was placed into a tube furnace preheated to 870 °C and maintained at that temperature for 10 hours. Finally, the furnace was left to cool down naturally to room temperature.

4.2 Synthesis and analysis of Sr_xCoO_2(SCONT)

In a typical synthesis of SCONTs, we started with 50 mg of $Sr_6Co_5O_{15}$ (SCOB) material. The bulk SCO was sonicated in a 5 M NaOH solution (by dissolving 4 g of NaOH in 20 mL of water) for 1 hour. After sonication, the reaction mixture was transferred into a sealed 25 mL autoclave and placed in an oven preheated to 220 °C. The autoclave was maintained at this temperature for 5 and 8 hours. For SCONT-5h, the autoclave was removed from the oven (at 220C) and immediately cooled using an ice bath. For SCONT-8h, after reaction is completed (8 hours) the autoclave was kept for cool down naturally to room temperature. Depending on the duration of the reaction time, the resulting nanotubes were labelled as SCONT-5h or SCONT-8h. Finally, the product was washed repeatedly with Milli-Q water until the wash water reached a neutral pH (7), then dried overnight at 60 °C. The dried powder was used for all subsequent characterizations.

4.3 Characterization techniques

Multiple characterization techniques were used to study the morphology, structure and composition of the synthesized material at the individual nanotube level, including scanning electron microscopy (SEM) (Zeiss Sigma-500), transmission electron microscopy (TEM) (Thermo Scientific, Themis 300 G3) and coupled with energy-dispersive X-ray spectroscopy (EDS) (Super-X detector). The phase was validated through powder XRD (Rigaku, $\lambda = 1.5418$ Å) and TEM analysis. To gain insights into the crystal structure, SAED and HRTEM analyses were performed using a Thermo Scientific instrument (Themis 300 G3 operated at 300 kV), which was equipped with a high-angle annular dark-field detector for STEM and utilized EDS with the Super-X detector. Chemical state analysis was conducted with an XPS instrument (Kratos Analytical, AXIS Supra). The XPS spectra were calibrated using C 1s spectra with the

peak at 284.8 eV, and peak fitting was done using a nonlinear Shirley background and a Gaussian × Lorentzian (70 % × 30 %).

4.4 Computational details

Spin-polarized density functional theory (DFT)[1] calculations are carried out within the projected augmented wave method (PAW)[2,3], implemented in the Vienna Ab-initio Simulation Package[4]. The exchange-correlation effects are captured using the Perdew-Burke-Ernzerhof (PBE) functional[5] within the generalized-gradient approach[6] with Sr, Co and O atoms having valence electronic configurations of $4s^2 4p^6 5s^2$, $3d^8 4s^1$, and $2s^2 2p^4$, respectively. We adopted the semiempirical Grimme's DFT-D3 dispersion correction[7,8] to account for the long-ranged van der Waals interactions. A Gaussian smearing with a width of 0.05 eV is adopted to carry out the electronic convergence. A kinetic energy cut-off of 480 eV is utilized to optimize a 2×2×2 supercell of bulk $SrCoO_2$, using a Γ-centered 4×4×1 k-mesh for the Brillouin zone sampling. A rotationally invariant DFT+U approach developed by Dudarev et al.[9] was adopted to treat the strongly correlated d-electrons of Cobalt with onsite corrections of U = 5 eV and J = 1 eV.[10–12] The energy and force convergence criteria are taken to be 1×10^{-5} eV and −0.02 eV $Å^{-1}$, respectively. To avoid spurious interactions, a vacuum of 15 Å is inserted along the perpendicular direction. In this as-generated surface slab, the number of Sr and Co atoms are unequal due to the CoO_2 termination applied to both the top and bottom surfaces. The CoO_2-terminated $SrCoO_2$ surface was chosen due to following reasons:

1. Previous studies report CoO_2 termination as the most stable surface of $LiCoO_2$.

2. Experimentally, CoO_2 acts as the active site for the OER mechanism.

3. Since Sr is intercalated between two CoO_2 layers, it cannot exist as an isolated surface layer. Thus, both slab ends were terminated with CoO_2, leading to an uneven Sr:Co ratio of 16:20.

After the structural optimization, the electronic density of states, electronic wavefunction, spin density and charge transfer are recalculated at higher 20×20×1 k-mesh. The spin and charge-transfer mechanism was investigated using the Bader charge analysis, a method developed by Henkelman[13,14]. The LOBSTER package[15,16] was utilized to perform the Crystal orbital Hamilton population (COHP) calculations to investigate the bonding mechanism.

Working Electrode Preparation and Electrochemical Characterization for OER

The OER performance of the synthesized samples (SCONT-5h, SCONT-8h, and bulk SCOB) were evaluated using a Metrohm Autolab PGSTAT302N potentiostat in a standard three-electrode configuration. All measurements were performed in O_2-saturated 0.5 M NaOH electrolyte at room temperature. Catalyst inks were prepared by dispersing 4 mg of sample and 1 mg of conductive carbon in 4.9 ml of DI water with 100 µL Nafion binder (5 wt%). The mixture was ultrasonicated for 30 minutes to make a homogeneous dispersion. A 5 µL aliquot of the prepared ink was drop-cast onto a mirror-polished glassy carbon electrode (GCE, 3 mm diameter, geometric area = 0.0707 cm^2) and dried under IR lamp.

The catalyst-modified glassy carbon electrode acting as the working electrode, a platinum wire as the counter electrode, and a Hg/HgO (1.0 M NaOH) electrode as the reference. Linear sweep voltammetry measurements were performed at a controlled scan rate of 2 mV s^{-1} and all the recorded potentials were converted to the reversible hydrogen electrode (RHE) scale using the relation:

$$E(RHE) = E(vs\ Hg/HgO) + 0.950\ V$$

Electrochemical double-layer capacitance (C_{dl}) was measured from cyclic voltammetry (CV) scans in a non-faradaic region (0 to 0.1V vs Hg/HgO) at various scan rates (20-50 mV s^{-1}). The slope of the current density vs. scan rate plot was used to estimate the electrochemically active surface area (ECSA), assuming a specific capacitance of 40 µF cm^{-2}.

The TOF values were calculated using the standard formula:[17]

$$\mathrm{TOF} = \frac{J * A}{4.n \cdot F}$$

where J is the current density at a given overpotential (in Amps/cm^2), A area in cm^2, n is the number of moles of active surface Co sites and F is Faraday's constant (96485 C/mol).

Electrochemical Measurements for Supercapacitor Performance Evaluation

Three-Electrode Configuration

Cyclic voltammetry (CV), galvanostatic charge-discharge (GCD) and EIS measurements were performed using a three-electrode setup in 1 M LiOH aqueous electrolyte. The working electrode was prepared by dispersing 2 mg of the active material in a mixture of 190 µL Milli-Q

water and 10 µL of Nafion solution (5 wt%). The mixture was sonicated for 30 minutes to make a homogeneous ink, subsequently, 5 µL of the ink was drop-cast onto the polished surface of the GCE and dried with IR lamp. A saturated calomel electrode (SCE) and a platinum wire were used as the reference and counter electrodes, respectively. Electrochemical measurements were performed within a potential window of –0.15 to 0.45 V vs. SCE at various scan rates.

The C_s (F g^{-1}) was calculated from the CV data using the equation:[18]

$$C_s = \frac{1}{\Delta V \times m \times v} \int_{V1}^{V2} I(V)dV \qquad (1)$$

Where V_1 and V_2 are the lower and upper potentials in the CV curves, $I(V)$ is the current at each potential, ΔV is the potential window, m is the mass of the active material, and v is the scan rate.

The capacitance (C_s) was calculated from the GCD curve using the equation:[19]

$$C_s = \frac{I \times t}{m \times \Delta V} \qquad (2)$$

Here I, t, m and ΔV are applied current, discharge time in seconds, active mass of material, and potential window, respectively.

Symmetric Two-Electrode Configuration

A symmetric supercapacitor was assembled in a Swagelok-type cell to evaluate the performance of SCONT-5h sample. The electrode ink was prepared by mixing 4 mg of SCONT-5h and 1 mg of conductive carbon black dispersed in 470 µL of deionized water with 30 µL of Nafion (5 % solution) as binder. The mixture was sonicated for 30 min to ensure homogeneity. The ink was then drop-cast onto a graphite sheet to achieve a mass loading of 1 mg per electrode, followed by drying at 60 ◦C for 12 h. Two identical electrodes were assembled in the Swagelok cell, separated by a glass fiber membrane soaked in 1 LiOH electrolyte. Electrochemical measurements, including CV, galvanostatic charge-discharge and EIS, were performed to assess the energy and power densities of the symmetric supercapacitor. Specific capacitance (C_s), power density (P_s) and energy density (E_s) of the SSC were estimated based on the GCD curves according to the following relations:[20,21]

$$C_s = 2 \times \frac{I \times t}{m \times \Delta V} \quad (\text{F g}^{-1})\text{.....(3)}$$

$$E_s = \frac{1}{2 \times 3.6} C_s \times (\Delta V)^2 \quad (\text{Wh/kg})\text{.....(4)}$$

$$P_s = \frac{3.6 \times E_s}{\Delta t} \quad (\text{kW/kg})\text{.....(5)}$$

Here, C_s is in F g^{-1},I is discharge current in amperes (A), t is discharge time in seconds(s) from GCD, m is mass active material of one electrodes in grams (g) and ΔV is the cell voltage after considering the internal resistance (IR) drop from the GCD curves.

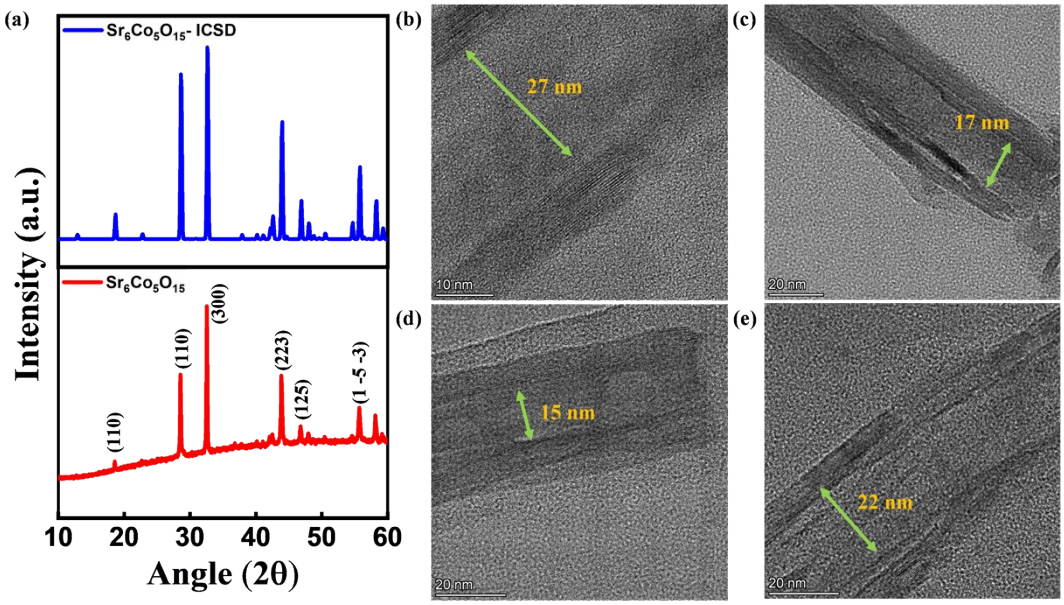

Figure S1. (a) Powder XRD patterns of as synthesized SCOB and $Sr_6Co_5O_{15}$ from ICSD (coll code 147246). b,c) inner diameter of SCONT-5h. (d,e) inner diameter of SCONT-8h.

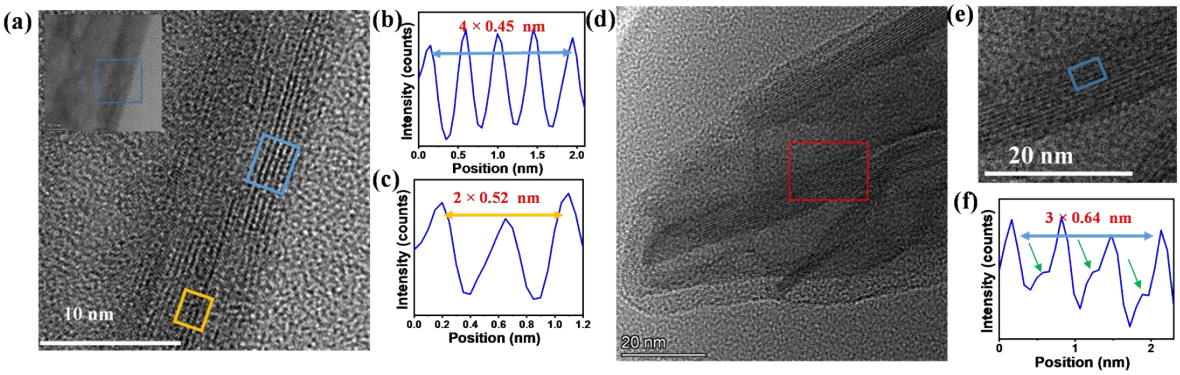

Figure S2. (a) HR-TEM image of SCONT-5h showing stacking fault along c direction. (b) Represent the line profile plot of area with d spacing of 0.45 nm. (c) Showing the line profile diagram of area marked with yellow rectangle which has slightly higher d spacing of 0.52 nm along c direction. HR-TEM image of SCONT-8h (d) and red marked area is further magnified in (e) and the corresponding line profile diagram is plotted in (f).

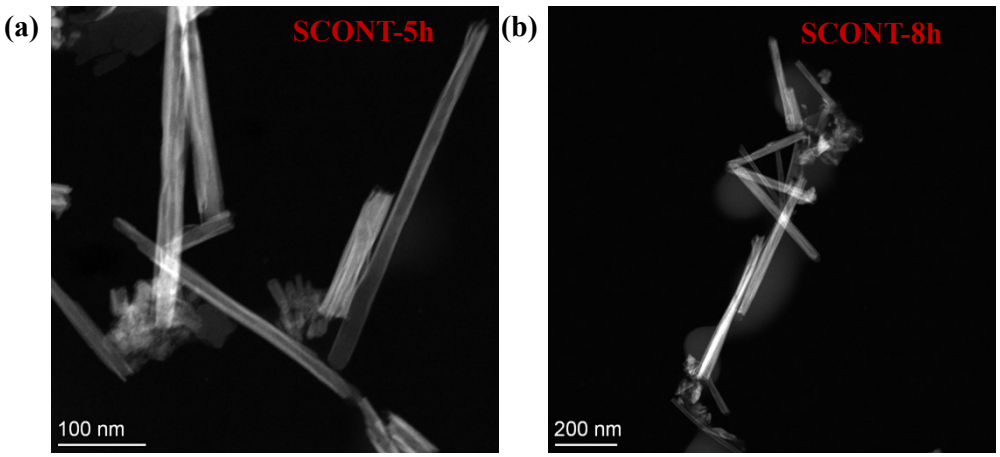

Figure S3. (a) HAADF image of SCONT-5h(a) and SCONT-8h(b)

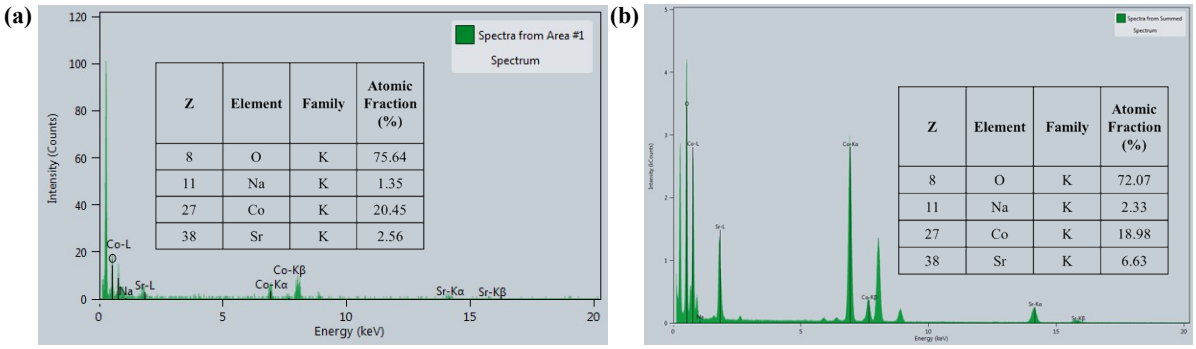

Figure S4. EDS spectrum and atomic composition of SCONT-5h (a) and SCONT-8h (b)

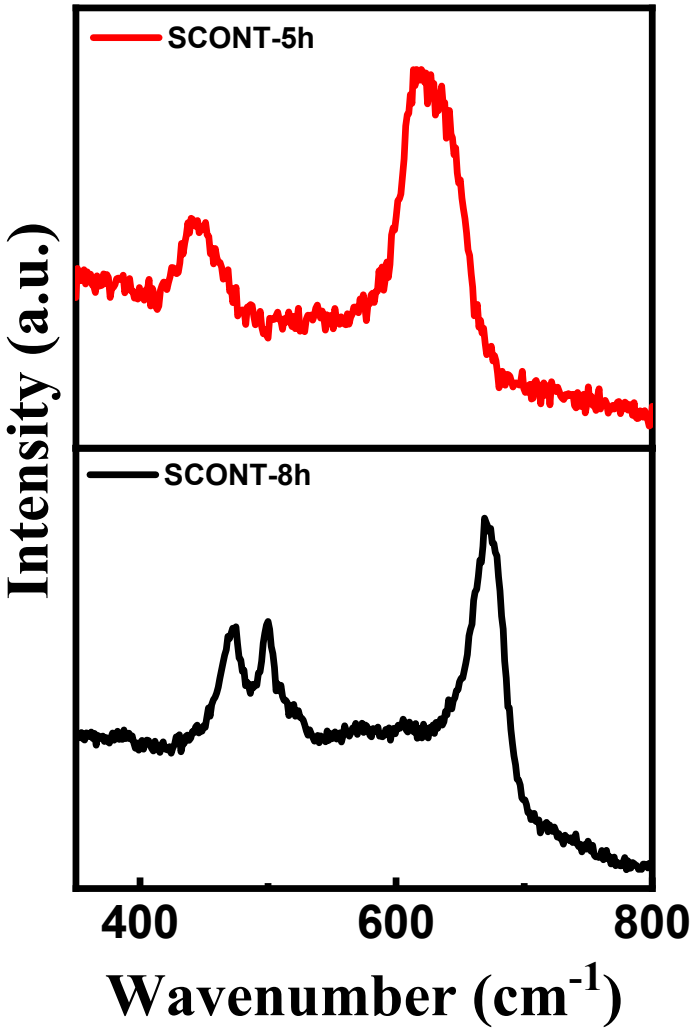

Figure S5: Raman spectra of the as-synthesized SCONT-5h and SCONT-8h nanotubes, showing the characteristic A_{1g} and E_g modes of the CoO_6 octahedra and their respective shifts with varying Sr intercalation.

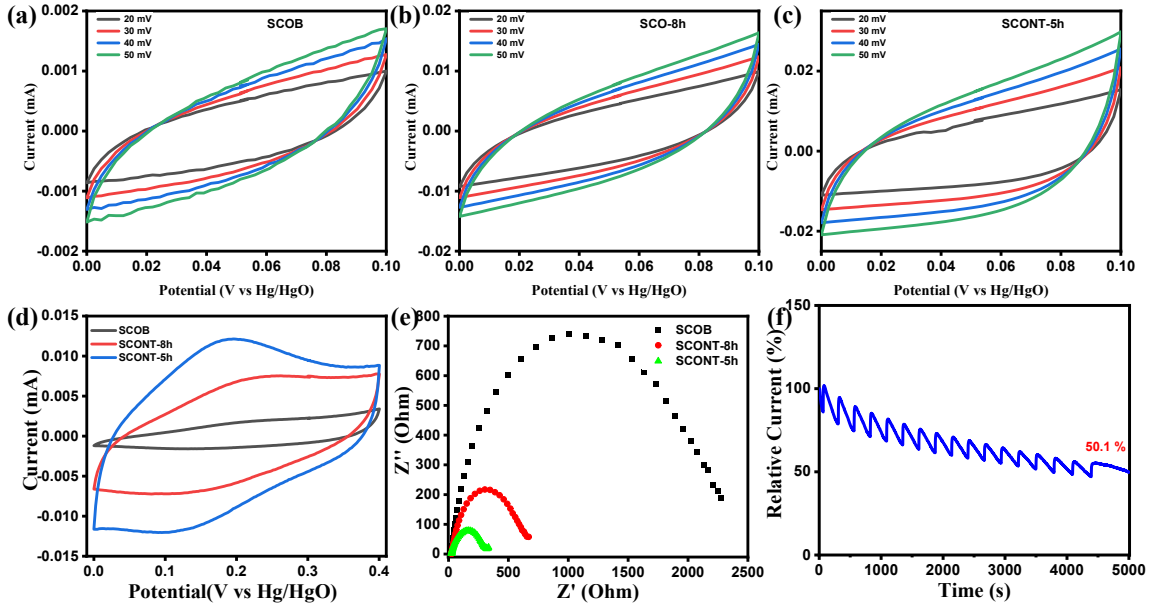

Figure S6. (a-c) CV curves recorded in the non-Faradaic region (0-0.1 V vs. Hg/HgO) at scan rates of 20-50 mV s^{-1} in 0.5 M NaOH, used for ECSA estimation of the respective samples. (d) CV comparison of the samples recorded in the Faradaic region, used to estimate the number of electrochemically active sites. (e) Electrochemical impedance spectra (EIS) of SCONT-5h, SCONT-8h, and SCOB catalysts. The SCONT-5h sample exhibits a significantly smaller high-frequency semicircle, corresponding to a lower charge transfer resistance (Rct ≈ 281 Ω), indicating that nanostructuring combined with low Sr intercalation effectively reduces Rct and enhances OER kinetics. (f) OER stability of SCONT-5h sample measured by the chronoamperometry measurement.

Ab-initio DFT calculations

Density functional theory (DFT) calculations are carried out to understand the changes in the Co-oxidation state and Co-O covalency with respect to the change in Sr-deficiency. $SrCoO_2$ shares the same structure as $LiCoO_2$, having $R\underline{3}m$ symmetry (space group 166), as shown in **Figure S8** of the supporting information (SI). Each Co^{+2} atom is connected octahedrally to six O atoms and each octahedron is corner shared with its neighbours. These octahedrally bound Co^{+2} atoms have high spin $3d^7$ electronic state with a magnetic moment of 2.68 μ_B. Sr^{+2} ions

are intercalated in between the 2D CoO_2 layers. At the DFT+U (U=5eV, J=1eV) level, the calculated hexagonal lattice parameters are a=b=3.219 Å and c=14.943Å. The interlayer and intralayer spacings are 1.806 Å and 3.176 Å, respectively. The CoO_2-terminated surface slab, as shown in **Figure S8c,** contains 19 atomic layers, and are separated by 15 Å of vacuum space along c-axis to avoid spurious interaction. To model Sr-deficient structures, Sr vacancies are created in the as-optimized surface slab of $SrCoO_2$ pristine structure (**Figure S9a**) and generate four structures with varying Sr concentrations viz., 93.75 at.% Sr, 87.5 at.% Sr, 81.25 at.% Sr (**Figure S9(b-e)**). These Sr-deficient structures were generated by creating 1 Sr vacancy (93.75 at.% Sr), 2 Sr vacancies (87.5 at.% Sr), and 3 Sr vacancies (81.25 at.% Sr) in a 2×2×2 supercell of pristine $SrCoO_2$, containing a total of 16 Sr atoms. There exist two energetically competing structures for 81.25 at.% Sr labelled as Type-I and Type II, and we have presented the results for both of them. The objective is to showcase a trend of variation of Co-oxidation state and Co-O covalency with respect to the increasing content of Sr-deficiency, rather than simulating the exact percentage of Sr-deficiency, as obtained experimentally (Co:Sr = 8:1 in SCONT-5h and Co:Sr=2.8:1 in SCONT-8h). Further computational details are given in the supporting information (SI).

The oxidation state of cobalt in many compounds is often estimated by analysing its magnetic moment, since the number of unpaired electrons, and hence the total spin depends directly on the oxidation state and electronic configuration of cobalt.[22–25] Cobalt commonly exists in the +2, +3, and occasionally +4 oxidation states, corresponding to $3d^7$, $3d^6$, and $3d^5$ electronic configurations, respectively. Each of these states gives rise to characteristic magnetic moments depending on whether the complex is in high-spin or low-spin states, which is governed by the octahedral/tetrahedral ligand field strength. Hence, by comparing the computationally derived Co magnetic moments with varying Sr-deficiency, we can infer the likely oxidation and spin state of cobalt in pristine and all Sr-deficient structures.

The magnetic moments of cobalt atoms in pristine $SrCoO_2$, 93.75 at.% Sr, 87.5 at.% Sr, 81.25 at.% Sr Type-I, and 81.25 at.% Sr Type-II deficient structures were estimated using the PBE+U approach (see **Table S4**). The calculated magnetic moments on different Co-sites vary between 0 μ_B and ~3 μ_B, indicating the coexistence of cobalt atoms in multiple oxidation and spin states. By correlating the computed magnetic moments with the expected oxidation state values reported in the literature[49,50], we assign the likely oxidation states as follows: Co^{2+} (high-spin (HS), ~3 μ_B), Co^{3+} (intermediate-spin (IS), ~2 μ_B; or low-spin (LS), ~0 μ_B), and Co^{4+} (low-spin, ~1 μ_B). In the pristine $SrCoO_2$ lattice, all Co sites exhibit nearly identical magnetic

moments of about 3 μ_B, consistent with a Co^{2+} high-spin ($3d^7$, S = 3/2) configuration. As shown in **Figure S7 (a-e)**, upon introducing Sr vacancy, the magnetic moments of specifically those Co atoms near the vacancy site, decrease systematically, reflecting progressive increase in oxidation state from $Co^{2+} \Rightarrow Co^{3+} \Rightarrow Co^{4+}$. This evolution may arise because Sr removal leads to depletion of electrons from the transition-metal–oxygen framework, reducing the overall electron count at cobalt sites. The resulting increase in crystal-field splitting (Δ) and enhanced covalency between Co-3d and O-2p orbitals favour spin pairing, thereby stabilizing low-spin Co^{3+} ($3d^6$, S = 0) and Co^{4+} ($3d^5$, S = 1/2) states. Similar spin-state transitions and oxidation-state redistributions have been reported experimentally in lithium-deficient and doped cobalt oxides.[26–29] These results confirm that magnetic moment analysis from DFT provides a consistent and chemically intuitive means of estimating the evolution of oxidation-state in experimentally observed Sr-rich (SCONT-8h) to Sr-deficient (SCONT-5h) structures.

The magnetic moment analysis of $SrCoO_2$ compounds reveals the presence of multiple oxidation states in cobalt, with a clear trend of increasing oxidation state as the Sr deficiency increases. This observation suggests a corresponding increase in covalency within the Co-O bonds, as higher oxidation states should typically enhance electron delocalization between metal and oxygen. To further substantiate the increase in covalency, we carefully analyze the simulated Bader charge, projected density of states (PDOS), and crystal orbital Hamilton population (COHP). The Bader charge analysis (**Table S3**) indicates that as Sr vacancies increase from pristine to 81.25 at. % Sr, the effective charge on cobalt decreases slightly from 1.221e to 1.161e, while the effective charge on oxygen becomes less negative, from -1.203e to -1.064e. This reduction in charge separation indicates enhanced electron sharing between Co and O, confirming stronger covalent interactions. Strontium normally acts as an electron charge donor in the lattice. Removing Sr reduces the Madelung potential, which destabilizes O^{2-} ions. This drives holes onto the O-2p states, causing oxygen to become less negative (i.e., O loses electrons).[30–32] These holes hybridize strongly with Co-3d orbitals, resulting in mixed cobalt oxidation states (Co^{2+}, Co^{3+}, Co^{4+}), mediated by enhancement in ligand-hole character due to increase in Sr-vacancies. Similar effect has previously been studied in $LiCoO_2$, wherein physical delithiation of epitaxial $LiCoO_2$ leads to formation of Co^{4+} near Li vacancies and the involvement of oxygen atoms with holes on O-2p states. This, in turn, indicates ligand-hole formation and enhanced Co-O covalency as revealed by their XPS and core-level analysis.[33] Other recent studies also support the presence of ligand-hole states in layered transition metal oxides including $LiCoO_2$. As such, the strong Co-O covalency and ligand-hole states play

crucial roles in redox activity and electrochemical performance of cathode behavior during delithiation cycles.[34,35] Concurrently, the simulated PDOS (as shown in **Figure S10**) also shows that the contribution of O-2p orbitals to the states near the Fermi level (E_f) increases significantly in 81.25 at. % Sr system as compared to pristine $SrCoO_2$. This increased presence of O-2p states at E_f implies that holes created by Sr deficiency are not localized solely on cobalt ions but also prominently reside on oxygen ligands. These ligand holes hybridize strongly with Co-3d orbitals as revealed via stronger Co-O orbital overlap, thus enhancing Co-O covalency in 81.25 at. % Sr system.The covalent bonding interaction between cobalt and oxygen atoms in $SrCoO_2$ arises due to significant overlap between Co-O orbitals. This orbital overlap facilitates electron sharing, which is a characteristic of covalent bonds. To quantitatively analyse this interaction, projected crystal orbital Hamilton population (pCOHP) is simulated. The pCOHP reflects bonding and antibonding contributions from specific atom pairs as a function of energy. By integrating the pCOHP values up to the Fermi energy (E_f), the obtained integrated COHP (ICOHP), serves as a quantitative measure of the covalent bond strength.

In **Figure S7 (f-k)**, ICOHP values are plotted for cobalt in various oxidation and spin states: high-spin Co^{2+} (HS), intermediate-spin Co^{3+} (IS), low-spin Co^{3+} (LS), and low-spin Co^{4+} (LS), in pristine $SrCoO_2$ and various Sr-deficient systems (93.75 at.% Sr, 87.5 at.% Sr, 81.25 at.% Sr Type-I, and 81.25 at.% Sr Type-II). The ICOHP values of pristine $SrCoO_2$ with Co^{2+} (HS) state (**Figure S7 f**) reveal bonding states extending below the Fermi energy (E_f), indicating covalent Co-O bond contributions mainly in the occupied states, with moderate bonding strength. **Figure S7 (g) and (h)** correspond to systems with 93.75 and 87.5 at.% Sr, respectively, containing mixed oxidation and spin states: Co^{3+} (IS) and Co^{2+} (HS). The ICOHP intensities increase compared to pristine, showing stronger Co-O covalency, and states closer to E_f suggest increasing metal-ligand hybridization. **Figure S7 (i,j,k)** show two types of 81.25 at.% Sr systems with four oxidation states Co^{4+} (LS), Co^{3+} (IS), Co^{3+} (LS), and Co^{2+} (HS). The ICOHP values for Sr-deficient systems (**Table S5**) indicate significantly enhanced bonding strengths, especially for Co^{4+}-O bond, demonstrated by largest negative ICOHP magnitudes below E_f. The presence of bonding states near E_f also signals strong hybridization and ligand-hole character.

Therefore, as the Sr concentration decreases from 93.75 at.% Sr to 81.25 at.% Sr, Co oxidation state progressively increases from Co^{2+} to Co^{4+}, and Co-O covalency simultaneously strengthens. This is evidenced by the growth in ICOHP magnitude (more negative values indicate stronger covalent interactions) and the shift of bonding states toward the Fermi level.

The increasing covalency suggests enhanced orbital overlap and hybridization between Co 3d and O 2p orbitals, which is characteristic of ligand-hole formation and charge redistribution upon oxidation. This is again consistent with the findings in $LiCoO_2$, wherein lithium extraction oxidizes Co ions, leading to stronger hybridization between Co-3d and O-2p orbitals, thus enhancing the covalent character.

Our comprehensive DFT analysis, comprising - the simulated magnetic moments, Bader charge, PDOS, and COHP demonstrates that Sr deficiency in $SrCoO_2$ induces multiple cobalt oxidation states, enhances Co-O covalency, and generates ligand-hole character. Magnetic moments reveal the presence of mixed $Co^{2+}/Co^{3+}/Co^{4+}$ states, while Bader charges quantify the decreasing ionicity of oxygen and formation of ligand (O)-holes. PDOS highlights increasing Co-3d and O-2p hybridization, and COHP confirms stronger Co-O bonding interactions. Together, these complementary theoretical analyses provide a unified picture of how stoichiometry variations modulate electronic structure, bonding, and covalency in layered oxides, offering key insights to substantiate our experimental claim of Co-oxidation and Co-O covalency enhancement with rise in Sr-deficiency.

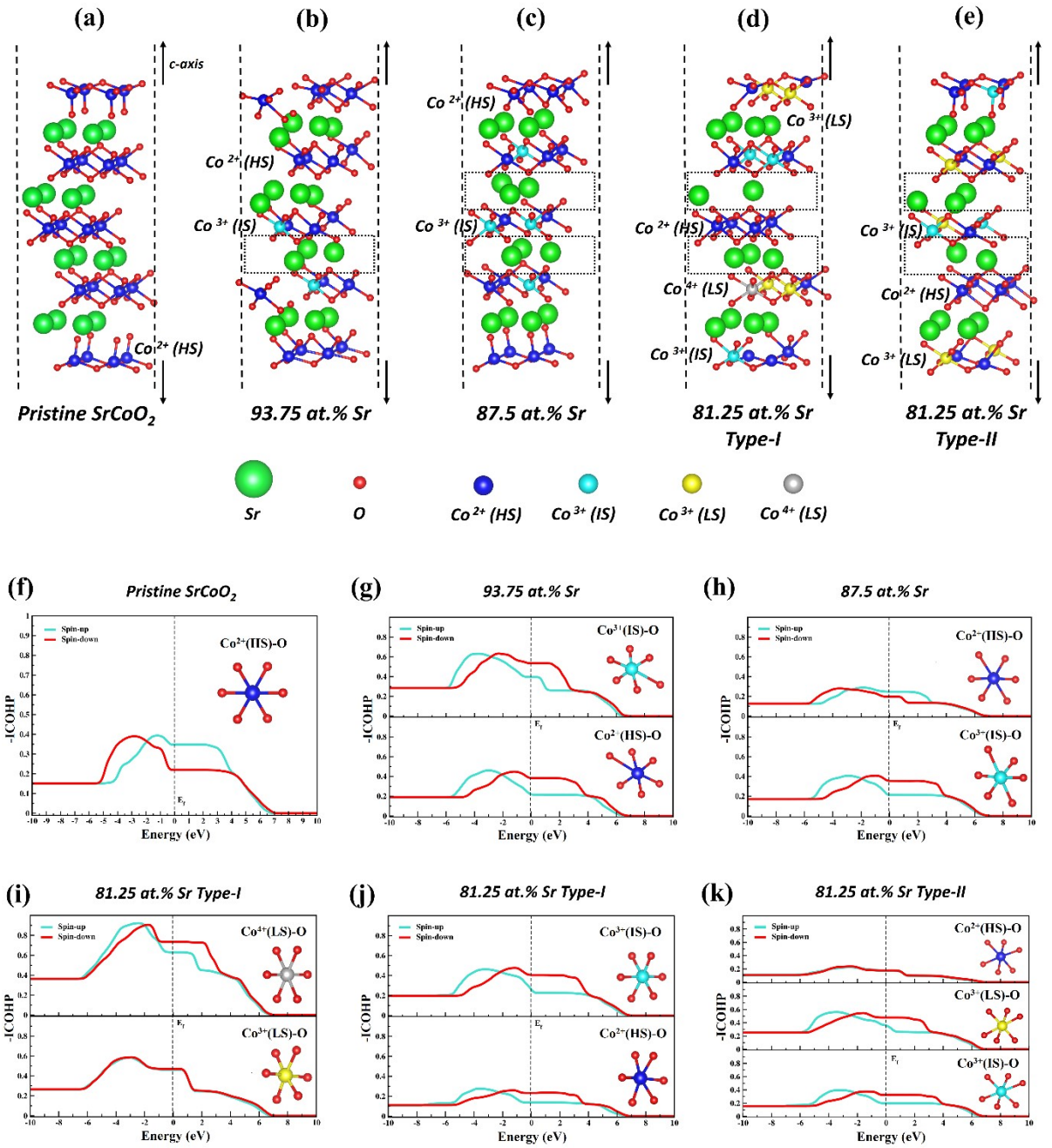

Figure S7: (a) CoO_2-terminated surface slab of $SrCoO_2$ pristine structure. **(b-e)** Sr-deficient structures removing 1 Sr (93.75 at. % Sr), 2 Sr (87.5 at. % Sr), and 3 Sr (81.25 at.% Sr Type-I and Type-II) with variable oxidation state of Co: Co^{2+} (high-spin (HS), $3d^7$), Co^{3+} (intermediate-spin (IS), $3d^6$) Co^{3+} (low-spin (LS), $3d^6$), and Co^{4+} (low-spin (LS), $3d^5$). Black dashed-lines indicate the hexagonal unit cell, while the black dotted-boxes indicate the positions where the Sr-vacancy is created. **(f-k)** Integrated crystal orbital Hamilton populations (ICOHP) for cobalt in various oxidation and spin states: high-spin Co^{2+} (HS), intermediate-spin Co^{3+} (IS), low-spin Co^{3+} (LS), and low-spin Co^{4+} (LS), corresponding to compositions from **(f)** (high-Sr) pristine $SrCoO_2$ to Sr-deficient systems (**(g)** 93.75 at.% Sr, **(h)** 87.5 at.% Sr, **(i,j)** 81.25 at.% Sr Type-I, and **(k)** 81.25 at.% Sr Type-II.

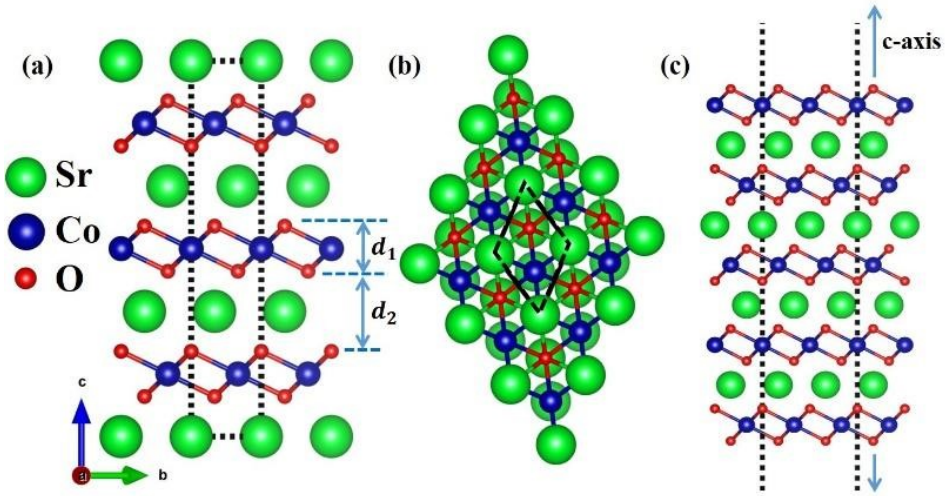

Figure S8: (a) Side and **(b)** top views of hexagonal bulk $SrCoO_2$ crystal structure and **(c)** its CoO_2-terminated surface slab containing 19 atomic layers. d_1 and d_2 are the vertical interplanar distance. Black dotted lines indicate the hexagonal unit cell.

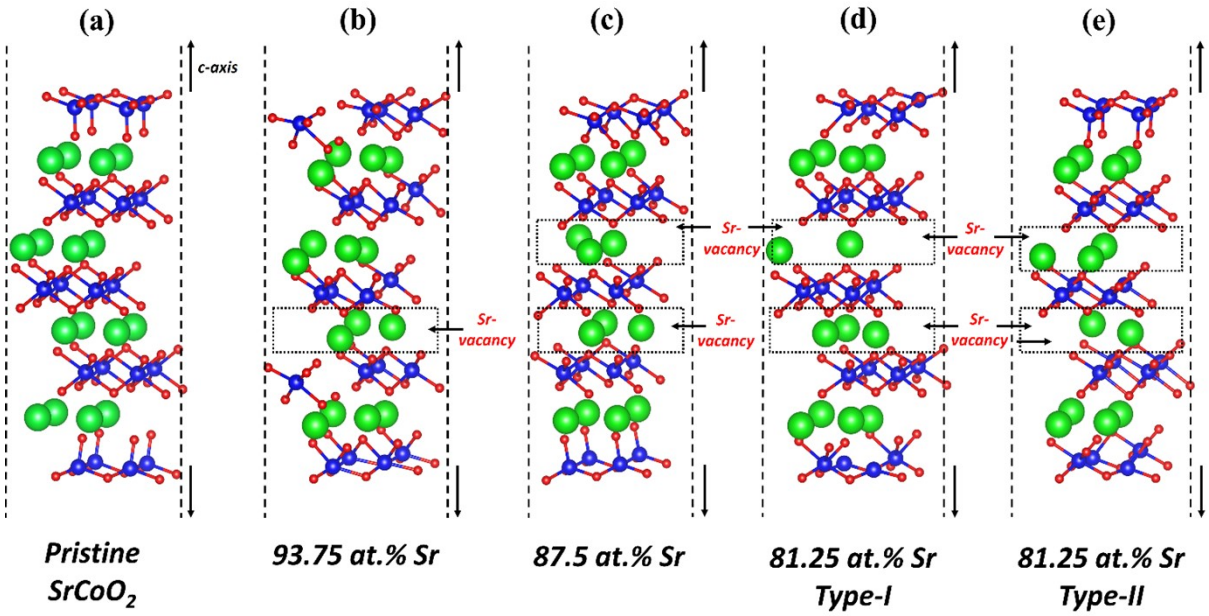

Figure S9: (a) Oxygen-terminated surface slab of pristine $SrCoO_2$ structure. **(b-e)** Sr-deficient structures with 1 Sr vacancy (93.75 at. % Sr), 2 Sr vacancies (87.5 at. % Sr), and 3 Sr vacancies (81.25 at.% Sr Type-I and Type-II). Type-I and Type-II are two energetically competing structural configurations for 81.25 at.% Sr case. Black dash lines indicate the hexagonal unit cell, while black dotted lines indicate the positions where Sr-vacancies are created.

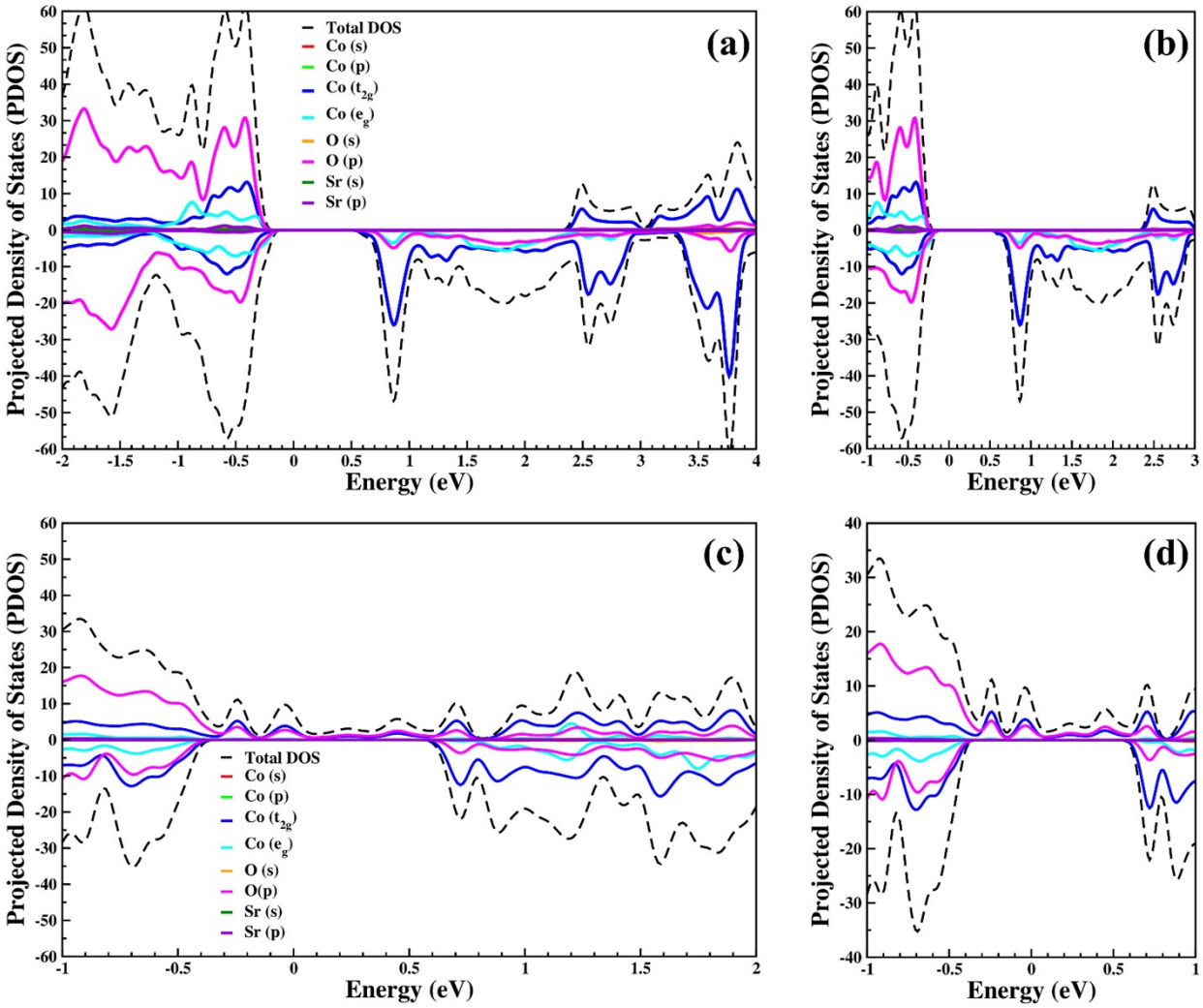

Figure S10: (a) Projected density of states (PDOS) of pristine $SrCoO_2$ surface slab. **(b)** Zoomed-in view of PDOS for pristine $SrCoO_2$ surface slab near Fermi level. **(c)** PDOS of 81.25 at.% Sr Type-II surface slab **(d)** Zoomed-in view of PDOS of 81.25 at.% Sr Type-II surface slab near Fermi level.

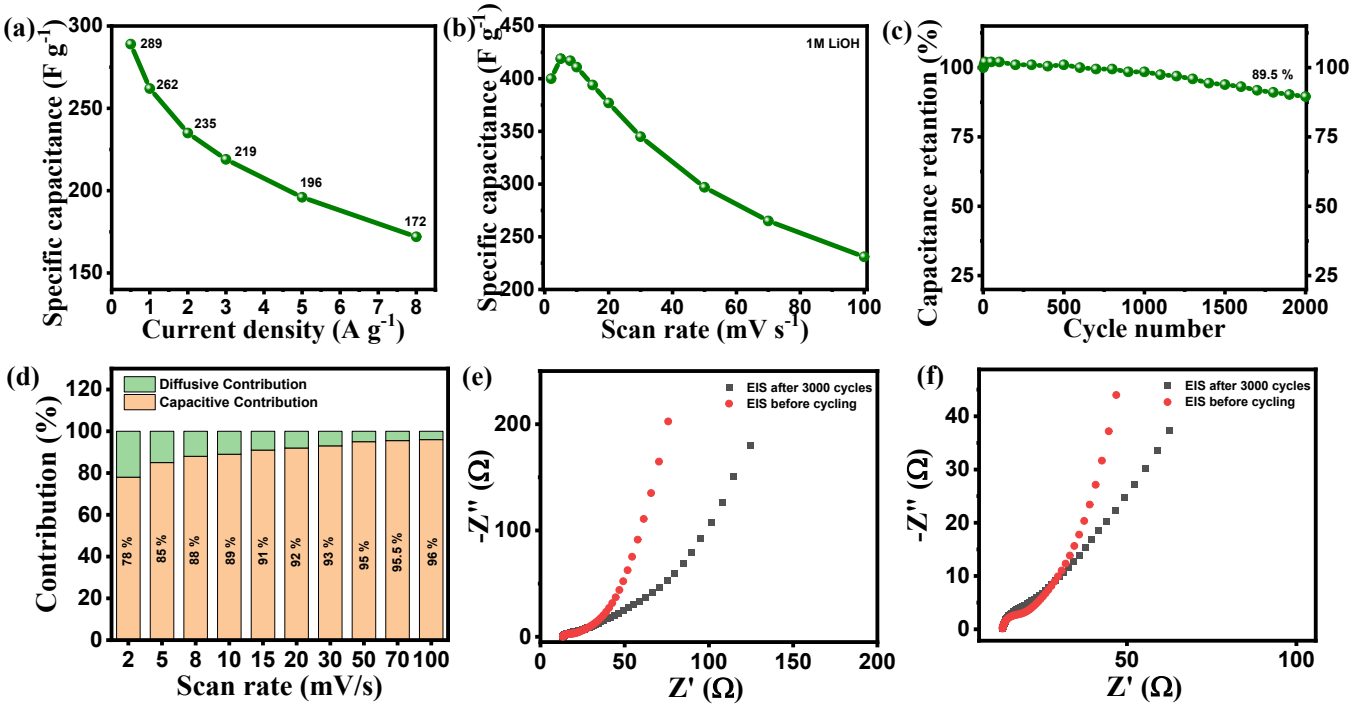

Figure S11. Specific capacitance of SCONT-5h in 1 M LiOH: (a) at different current densities, calculated from GCD curves; (b) at various scan rates, calculated from CV curves. (c) cyclic stability of SCONT-5h in SSC at constant current density of 3 A g^{-1} .. (d) Dunn's method analysis showing increasing capacitive contribution (77–94 %) with scan rate (2-100 mV s^{-1}), confirming surface-dominated charge storage with a minor diffusive component. (e-f) Nyquist plots before and after 3000 cycles showing slight increase in R_{ct}.

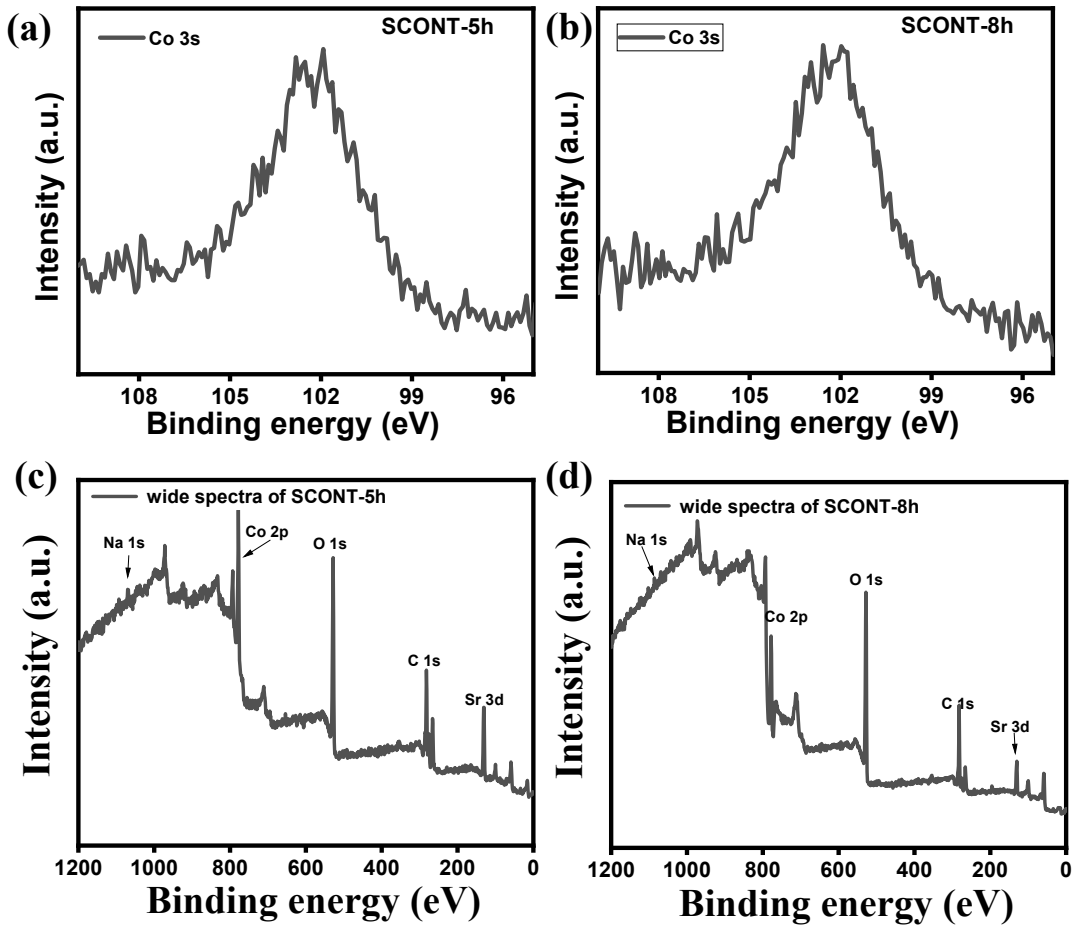

Figure S12. The core Co 3s spectra of SCONT-5h(a) and SCONT-8h(b). Wide XPS spectra of SCONT-5h(c) and SCONT-8h(d)

Table S1. (a) Electrochemically active surface area (ECSA) of the catalysts estimated from CV in the non-Faradaic region; (b) Turnover frequency (TOF) of the catalysts; (c) Number of active sites estimated from CV measurements in the Faradaic region.

(a)

Samples	ECSA(cm^2)
SCOB	1.17E-01
SCONT-8h	3.41E+00
SCONT-5h	3.26E+00

(b)

Samples	TOF (s^{-1})
SCOB	15.2
SCONT-8h	6.5
SCONT-5h	2.8

(c)

Samples	No. of active sites
SCOB	5.96676E+11
SCONT-8h	2.58393E+12
SCONT-5h	4.12556E+12

Table S2. XPS data comparison of SCONT-5h and SCONT-8h: (a) Co $2p_{3/2}$ peak, (b) Co 3p, (c) Co 3s, and (d) O 1s peak.

(a)

Co 2p3/2	Co^{3+}		Co^{3+}/ Co^{4+}		Co^{4+}	
	BE (eV)	Area %	BE (eV)	Area %	BE (eV)	Area %
SCONT-5h	779.7	49.14	781	42.61	783.5	8.24
SCONT-8h	779.40	62.9	780.8	25.7	782.5	11.3

(b)

Co 3p	Main peak	Sat. Peak
	Area %	Area %
SCONT 5h	88.7	11.3
SCONT 8h	86	14

(c)

Co 3s	FWHM (eV)
SCONT 5h	3.86
SCONT 8h	3.87

(d)

O 1s	O1		O2		O2/ O1
	BE (eV)	Area %	BE (eV)	Area %	
SCONT-5h	529.4	31.1	530.8	54.2	1.74
SCONT-8h	529	45.7	530.6	44.6	0.97

Table S3: ***Bader charge analysis.*** Average effective Bader charge (Z-Q) on Co and O atoms in pristine, 93.75 at. % Sr, 87.5 at. % Sr, 81.25 at. % Sr Type-I, and 81.25 at. % Sr Type-II structures.

Elements	Average Z-Q (effective charge)				
	Pristine	93.75 at. % Sr	87.5 at. % Sr	81.25 at. % Sr Type-I	81.25 at. % Sr Type-II
Co	1.221	1.21	1.183	1.176	1.161
O	-1.203	-1.163	-1.119	-1.065	-1.064

Table S4: Simulated magnetic moments on various Co-atoms in pristine, 93.75 at. % Sr, 87.5 at. % Sr, 81.25 at. % Sr Type-I, and 81.25 at. % Sr Type-II structures, with their likely oxidation and spin states.

Pristine $SrCoO_2$			93.75 at. % Sr			87.5 at. % Sr		
Element	Magnetic moment (μ_B)	Likely oxidation state	Element	Magnetic moment (μ_B)	Likely oxidation state	Element	Magnetic moment (μ_B)	Likely oxidation state
Co1	2.67	Co^{2+} (HS)	**Co1**	2.64	Co^{2+} (HS)	**Co1**	2.66	Co^{2+} (HS)
Co2	-2.67	Co^{2+} (HS)	**Co2**	2.64	Co^{2+} (HS)	**Co2**	-2.66	Co^{2+} (HS)
Co3	3.03	Co^{2+} (HS)	**Co3**	3.00	Co^{2+} (HS)	**Co3**	3.04	Co^{2+} (HS)
Co4	2.67	Co^{2+} (HS)	**Co4**	2.65	Co^{2+} (HS)	**Co4**	2.67	Co^{2+} (HS)
Co5	-2.67	Co^{2+} (HS)	**Co5**	1.91	Co^{3+}(IS)	**Co5**	-1.98	Co^{3+}(IS)
Co6	3.03	Co^{2+} (HS)	**Co6**	3.02	Co^{2+} (HS)	**Co6**	3.04	Co^{2+} (HS)
Co7	2.67	Co^{2+} (HS)	**Co7**	2.65	Co^{2+} (HS)	**Co7**	2.66	Co^{2+} (HS)
Co8	-2.67	Co^{2+} (HS)	**Co8**	2.63	Co^{2+} (HS)	**Co8**	-2.66	Co^{2+} (HS)
Co9	3.03	Co^{2+} (HS)	**Co9**	3.00	Co^{2+} (HS)	**Co9**	3.04	Co^{2+} (HS)
Co10	2.67	Co^{2+} (HS)	**Co10**	1.92	Co^{3+}(IS)	**Co10**	1.95	Co^{3+}(IS)
Co11	-2.67	Co^{2+} (HS)	**Co11**	2.64	Co^{2+} (HS)	**Co11**	-1.96	Co^{3+}(IS)
Co12	3.03	Co^{2+} (HS)	**Co12**	3.00	Co^{2+} (HS)	**Co12**	3.04	Co^{2+} (HS)
Co13	3.03	Co^{2+} (HS)	**Co13**	3.01	Co^{2+} (HS)	**Co13**	3.03	Co^{2+} (HS)
Co14	2.67	Co^{2+} (HS)	**Co14**	2.62	Co^{2+} (HS)	**Co14**	1.97	Co^{3+}(IS)
Co15	3.03	Co^{2+} (HS)	**Co15**	3.06	Co^{2+} (HS)	**Co15**	3.02	Co^{2+} (HS)
Co16	2.67	Co^{2+} (HS)	**Co16**	-2.61	Co^{2+} (HS)	**Co16**	-2.66	Co^{2+} (HS)
Co17	3.03	Co^{2+} (HS)	**Co17**	3.06	Co^{2+} (HS)	**Co17**	3.03	Co^{2+} (HS)
Co18	2.67	Co^{2+} (HS)	**Co18**	-2.61	Co^{2+} (HS)	**Co18**	-2.66	Co^{2+} (HS)
Co19	3.03	Co^{2+} (HS)	**Co19**	3.00	Co^{2+} (HS)	**Co19**	3.03	Co^{2+} (HS)
Co20	2.67	Co^{2+} (HS)	**Co20**	2.62	Co^{2+} (HS)	**Co20**	-2.66	Co^{2+} (HS)

81.25 at. % Sr Type-I			81.25 at. % Sr Type-II		
Element	**Magnetic moment (μ_B)**	**Likely oxidation state**	**Element**	**Magnetic moment (μ_B)**	**Likely oxidation state**
Co1	2.64	Co^{2+} (HS)	**Co1**	3.05	Co^{2+} (HS)
Co2	3.07	Co^{2+} (HS)	**Co2**	-0.03	Co^{3+}(S)
Co3	2.79	Co^{2+} (HS)	**Co3**	-2.94	Co^{2+} (HS)
Co4	0.00	Co^{3+}(LS)	**Co4**	2.68	Co^{2+} (HS)
Co5	2.69	Co^{2+} (HS)	**Co5**	2.14	Co^{3+}(IS)
Co6	2.07	Co^{3+}(IS)	**Co6**	0.00	Co^{3+}(LS)
Co7	0.00	Co^{3+}(LS)	**Co7**	2.70	Co^{2+} (HS)
Co8	3.09	Co^{2+} (HS)	**Co8**	2.14	Co^{3+}(IS)
Co9	3.01	Co^{2+} (HS)	**Co9**	0.01	Co^{3+}(LS)
Co10	0.94	Co^{4+}(LS)	**Co10**	3.05	Co^{2+} (HS)
Co11	3.07	Co^{2+} (HS)	**Co11**	2.63	Co^{2+} (HS)
Co12	2.80	Co^{2+} (HS)	**Co12**	2.94	Co^{2+} (HS)
Co13	2.93	Co^{2+} (HS)	**Co13**	3.01	Co^{2+} (HS)
Co14	2.47	Co^{3+}(IS)	**Co14**	2.64	Co^{2+} (HS)
Co15	0.02	Co^{3+}(LS)	**Co15**	-2.55	Co^{3+}(IS)
Co16	3.08	Co^{2+} (HS)	**Co16**	0.00	Co^{3+}(LS)
Co17	0.01	Co^{3+}(LS)	**Co17**	3.01	Co^{2+} (HS)
Co18	2.64	Co^{2+} (HS)	**Co18**	0.00	Co^{3+}(LS)
Co19	-2.94	Co^{2+} (HS)	**Co19**	3.00	Co^{2+} (HS)
Co20	2.54	Co^{3+}(IS)	**Co20**	2.66	Co^{2+} (HS)

Table S5: Integrated Crystal Orbital Hamilton Population (ICOHP) analysis of Co-O bond for each of the Co-site with variable oxidation state for pristine $SrCoO_2$**,** 93.75 at. % Sr, 87.5 at. % Sr, 81.25 at. % Sr Type-I, and 81.25 at. % Sr Type-II $SrCoO_2$ structures.

System	Co site index	Likely Oxidation state	ICOHP (Spin Up)	ICOHP (Spin Down)	ICOHP Sum
Pristine	Co5	Co^{2+} (HS)	-0.66375	-0.42679	-1.09054
93.75 at. % Sr	Co5	Co^{3+} (IS)	-2.36878	-3.20365	-5.57243
	Co7	Co^{2+} (HS)	-1.3084	-2.29487	-3.60327
87.5 at. % Sr	Co5	Co^{3+} (IS)	-1.27407	-2.12727	-3.40134
	Co7	Co^{2+} (HS)	-1.47754	-1.18573	-2.66327
81.25 at. % Sr Type-I	Co5	Co^{2+} (HS)	-0.81621	-1.39437	-2.21058
	Co7	Co^{3+} (LS)	-2.77728	-2.82509	-5.60237
	Co10	Co^{4+} (LS)	-3.78376	-4.41506	-8.19882
	Co14	Co^{3+} (IS)	-1.58359	-2.43315	-4.01674
81.25 at. % Sr Type-II	Co5	Co^{3+} (IS)	-1.20062	-1.94214	-3.14276
	Co7	Co^{2+} (HS)	-1.04668	-1.06214	-2.10882
	Co18	Co^{3+} (LS)	-2.15393	-2.86908	-5.02301

Table S6: Comparison of energy storage performance of SCONT-5h with representative cobalt-based and intercalated oxide electrode materials for supercapacitors.

Electrode Material	**Electrolyte**	**Type of SC**	**Maximum Energy Density (Wh/kg)**	**Ref.**
Co,N-doped CP	6 M KOH	Asymmetric	9.1	[36]
Co based film	1 M LiOH	Asymmetric	17	[37]
Mn-doped Co_3O_4	3 M KOH	Asymmetric	33	[38]
Co_3O_4 nanosheets	3 M KOH	Asymmetric	22.51	[39]
$CaCoO_2$-CoO_2 nanosheets	1 M LiOH	Symmetric	28.5	[40]
SCONT-5h	1 M LiOH	Symmetric	21.5	This work

References

1 P. Hohenberg, and W. Kohn, "Inhomogeneous Electron Gas," Phys. Rev. **136**(3B), B864–B871 (1964).

2 P. E. Blöchl, *Phys. Rev. B*, 1994, **50**, 17953–17979.

3 G. Kresse and D. Joubert, *Phys. Rev. B*, 1999, **59**, 1758–1775.

4 G. Kresse and J. Furthmüller, *Phys. Rev. B*, 1996, **54**, 11169–11186.

5 J. P. Perdew, K. Burke and M. Ernzerhof, *Phys. Rev. Lett.*, 1996, **77**, 3865–3868.

6 J. P. Perdew and W. Yue, *Phys. Rev. B*, 1986, **33**, 8800–8802.

7 J. Klimeš, D. R. Bowler and A. Michaelides, *Phys. Rev. B*, 2011, **83**, 195131.

8 M. Dion, H. Rydberg, E. Schröder, D. C. Langreth and B. I. Lundqvist, *Phys. Rev. Lett.*, 2004, **92**, 246401.

9 S. L. Dudarev, G. A. Botton, S. Y. Savrasov, C. J. Humphreys and A. P. Sutton, *Phys. Rev. B*, 1998, **57**, 1505–1509.

10 L. S. Panchakarla, L. Lajaunie, A. Ramasubramaniam, R. Arenal and R. Tenne, *Chem. Mater.*, 2016, **28**, 9150–9157.

11 J. D. Baran, M. Molinari, N. Kulwongwit, F. Azough, R. Freer, D. Kepaptsoglou, Q. M. Ramasse and S. C. Parker, *J. Phys. Chem. C*, 2015, **119**, 21818–21827.

12 A. Rébola, R. F. Klie, P. Zapol and S. Öğüt, *Appl. Phys. Lett.*, DOI:10.1063/1.4885389.

13 G. Henkelman, A. Arnaldsson and H. Jónsson, *Comput. Mater. Sci.*, 2006, **36**, 354–360.

14 R. F. W. Bader, *Acc. Chem. Res.*, 1985, **18**, 9–15.

15 R. Dronskowski and P. E. Blochl, *J. Phys. Chem.*, 1993, **97**, 8617–8624.

16 S. Maintz, V. L. Deringer, A. L. Tchougréeff and R. Dronskowski, *J. Comput. Chem.*, 2016, **37**, 1030–1035.

17 H. Qian, J. Wei, C. Yu, F. Tang, W. Jiang, D. Xia and L. Gan, *ACS Catal.*, 2022, **12**, 14280–14289.

18 A. S. Pillai, R. Rajagopalan, A. Amruthalakshmi, J. Joseph, A. Ajay, I. Shakir, S. V. Nair and A. Balakrishnan, *Colloids Surfaces A Physicochem. Eng. Asp.*, 2015, **470**, 280–289.

19 W. Chu, Z. Shi, Y. Hou, D. Ma, X. Bai, Y. Gao and N. Yang, *ACS Appl. Mater. Interfaces*, 2020, **12**, 2763–2772.

20 S. P. Gupta, A. R. Shakeelur Raheman, A. Gurung, Q. Qiao, D. J. Late and P. S. Walke, *Carbon N. Y.*, 2022, **192**, 153–161.

21 Y. Lu, N. Chen, Z. Bai, H. Mi, C. Ji and L. Sun, *ACS Sustain. Chem. Eng.*, 2018, **6**, 14838–14846.

22 S. Y. Istomin, O. A. Tyablikov, S. M. Kazakov, E. V. Antipov, A. I. Kurbakov, A. A.

Tsirlin, N. Hollmann, Y. Y. Chin, H.-J. Lin, C. T. Chen, A. Tanaka, L. H. Tjeng and Z. Hu, *Dalt. Trans.*, 2015, **44**, 10708–10713.

23 M. C. Viola, M. J. Martínez-Lope, J. A. Alonso, J. L. Martínez, J. M. De Paoli, S. Pagola, J. C. Pedregosa, M. T. Fernández-Díaz and R. E. Carbonio, *Chem. Mater.*, 2003, **15**, 1655–1663.

24 V. P. Plakhty, P. J. Brown, B. Grenier, S. V. Shiryaev, S. N. Barilo, S. V. Gavrilov and E. Ressouche, *J. Phys. Condens. Matter*, 2006, **18**, 3517–3525.

25 G. J. Shu and F. C. Chou, *Phys. Rev. B*, 2016, **93**, 140402.

26 J. T. Hertz, Q. Huang, T. McQueen, T. Klimczuk, J. W. G. Bos, L. Viciu and R. J. Cava, *Phys. Rev. B*, 2008, **77**, 075119.

27 F. Gendron, S. Castro-garcia, E. Popova and S. Ziolkiewicz, 2003, **157**, 125–132.

28 F. Khatun, M. A. Gafur, M. S. Ali, M. S. Islam and M. A. R. Sarker, *J. Sci. Res.*, 2014, **6**, 217–231.

29 S. Levasseur, *Solid State Ionics*, 2000, **128**, 11–24.

30 D. Koch and S. Manzhos, *J. Phys. Chem. C*, 2020, **124**, 19962–19968.

31 Z. Zhou, C. Cazorla, B. Gao, H. D. Luong, T. Momma and Y. Tateyama, *ACS Appl. Mater. Interfaces*, 2023, **15**, 53614–53622.

32 A. K. Varanasi, A. Bhowmik, T. Sarkar, U. V. Waghmare and M. D. Bharadwaj, *Ionics (Kiel).*, 2014, **20**, 315–321.

33 E. Salagre, P. Segovia, M. Á. González-Barrio, M. Jugovac, P. Moras, I. Pis, F. Bondino, J. Pearson, R. S. Wang, I. Takeuchi, E. J. Fuller, A. A. Talin, A. Mascaraque and E. G. Michel, *ACS Appl. Mater. Interfaces*, 2023, **15**, 36224–36232.

34 Y. Lyu, X. Wu, K. Wang, Z. Feng, T. Cheng, Y. Liu, M. Wang, R. Chen, L. Xu, J. Zhou, Y. Lu and B. Guo, *Adv. Energy Mater.*, 2021, **11**, 1–29.

35 H. Huang, Y.-C. Chang, Y.-C. Huang, L. Li, A. C. Komarek, L. H. Tjeng, Y. Orikasa, C.-W. Pao, T.-S. Chan, J.-M. Chen, S.-C. Haw, J. Zhou, Y. Wang, H.-J. Lin, C.-T. Chen, C.-L. Dong, C.-Y. Kuo, J.-Q. Wang, Z. Hu and L. Zhang, *Nat. Commun.*, 2023, **14**, 2112.

36 A. K. Díaz-Duran, G. Montiel, F. A. Viva and F. Roncaroli, *Electrochim. Acta*, 2019, **299**, 987–998.

37 R. Deka, S. Rathi and S. M. Mobin, *Energy Adv.*, 2023, **2**, 2119–2128.

38 J. Wang, H. Zhang, H. Duan, H. Zhao, J. Qi, B. Ma and H. Fan, *ACS Omega*, 2024, **9**, 6955–6964.

39 A. Umar, S. D. Raut, A. A. Ibrahim, H. Algadi, H. Albargi, M. A. Alsaiari, M. S. Akhtar, M. Qamar and S. Baskoutas, *Electrochim. Acta*, 2021, **389**, 138661.

40 R. K. Mohanta, S. P. Gupta, A. Yella and L. S. Panchakarla, *ACS Electrochem.*, 2025, **1**, 633–644.